Superradiance induced multistability in one-dimensional driven Rydberg lattice gases

Yunhui He[⋆,1], Zhengyang Bai[⋆,2,4], Yuechun Jiao[1,4], Jianming Zhao[1,4,*] and Weibin Li[3†]
[1] *State Key Laboratory of Quantum Optics and Quantum Optics Devices, Institute of Laser Spectroscopy, Shanxi University, Taiyuan 030006, China*
[2] *State Key Laboratory of Precision Spectroscopy, East China Normal University, Shanghai 200062, China*
[3] *School of Physics and Astronomy, and Centre for the Mathematics and Theoretical Physics of Quantum Non-equilibrium Systems, University of Nottingham, Nottingham, NG7 2RD, UK*
[4] *Collaborative Innovation Center of Extreme Optics, Shanxi University, Taiyuan 030006, China*

We study steady state phases of a one-dimensional array of Rydberg atoms coupled by a microwave (MW) field where the higher energy Rydberg state decays to the lower energy one via single-body and collective (superradiant) decay. Using mean-field approaches, we examine the interplay among the MW coupling, intra-state van der Waals (vdW) interaction, and single-body and collective dissipation between Rydberg states. A linear stability analysis reveals that a series of phases, including uniform, antiferromagnetic, oscillatory, and bistable and multistable phases can be obtained. Without the vdW interaction, only uniform phases are found. In the presence of the vdW interaction, multistable solutions are enhanced when increasing the strength of the superradiant decay rate. Our numerical simulations show that the bistable and multistable phases are stabilized by superradiance in a long chain. The critical point between the uniform and multistable phases and its scaling with the atom number is obtained. Through numerically solving the master equation of a finite chain, we show that the mean-field multistable phase could be characterized by expectation values of Rydberg populations and two-body correlations between Rydberg atoms in different sites.

I. INTRODUCTION

Collective behaviors are intriguing in various many-body systems and attract intensive interest currently. Among them, superradiance is a cooperative radiation effect in dense atomic samples [1]. Spontaneous decay of individual atoms occurs due to fluctuations of vacuum fields surrounding atoms. When interatomic separation R_{jk} is smaller than wavelength λ of the respective transition, i.e. the Dicke limit $R_{jk} \ll \lambda$ [2], decay becomes collective such that its rate depends on the number of atoms in the ensemble, and hence can be much larger than the individual decay rate [3]. Since predicted by Dicke, superradiance has been confirmed in a variety experimental settings including Rydberg atoms [4–8], cavities [9–11], Bose-Einstein condensates [12–14], and quantum dots [15]. On the other hand, insights gained from the study of superradiance allow us to develop applications in quantum metrology [16, 17], narrow linewidth lasers [18–20] and atomic clocks [21], etc.

Rydberg atoms become an ideal platform for studying superradiance because of their millimeter-wavelength energy intervals, inherent dissipation [5, 22], and spatial configurability [23–25]. Rydberg atoms have extremely large electric dipole transition moments that can cause strong and long-range interactions of Rydberg states. There have been numerous theoretical and experimental investigations on the competition between dissipation and strong Rydberg atom interactions [26–35]. The strong interaction between Rydberg atoms leads to blockade effects [36–39]. Taking into account of single-body dissipation, novel phases [40–42] and critical behaviors [26, 43–46] emerge in such driven-dissipation many-body setting. We have recently experimentally observed blackbody radiation enhanced superradiance of ultracold Rydberg atoms in a magneto-optical trap (MOT) [8]. In a cold gas of dense Rydberg atoms, decay from $|nD\rangle$ state to $|(n+1)P\rangle$ state is much faster than the single-body decay rate, which is identified to be superradiant. It is found that the strong van der Waals (vdW) interaction between Rydberg atoms plays crucial roles. The interplay between superradiance and vdW interactions affects the many-body dynamics as well as scaling of the superradiance with respect to number N of Rydberg atoms.

In this work, we study superradiance between two Rydberg states in a 1D lattice (see Fig. 1), where atoms experience strong vdW interactions and are coupled by a microwave field. This lattice setting allows us to explore superradiance between Rydberg states in a controllable fashion, e.g. modifying the effective collective dissipation and interaction strength between Rydberg atoms by changing the atomic density and principal quantum number. Dynamics of the driven-dissipative Rydberg lattice is governed by a Lindblad master equation. We first establish mean-field phase diagrams as a function of external drive and detuning. We find a variety of sta-

⋆ These two authors contributed equally to this work.
* zhaojm@sxu.edu.cn
† weibin.li@nottingham.ac.uk

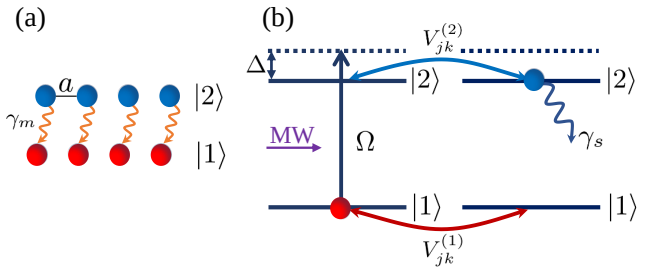

Figure 1. 1D array of interacting Rydberg atoms. (a) A large number of atoms are fixed on the 1D lattice. a is the lattice distance and γ_m is the many-body decay term. (b) the energy level of our model. A microwave field with Rabi frequency Ω drives atoms from $|1\rangle$ to $|2\rangle$. $\Delta = \omega - \omega_0$ is the detuning from the two-level transition ω_0. γ_s is the single-body decay term and $V_{jk}^{(1)}(V_{jk}^{(2)})$ is the vdW interaction between the same state $|1\rangle(|2\rangle)$ when atoms in site j and k.

tionary phases, including antiferromagnetic, oscillatory, phase bistabilities, and multistabilities. We show that Rydberg superradiance leads to multistable phases that are absent in previous studies [47]. In a finite chain, we obtain steady states by numerically solving the master equation. Two-body correlations and Rydberg populations exhibit different features in the corresponding mean-field phases, and could signify the emergence of bistable and multistable phases.

The paper is organized as follows. In Sec. II, we describe master equation of the Rydberg atoms on a 1D lattice. In Sec. III, we use mean-field theory and ansatz to analyze steady states of the model. Different phases, described by order parameter S_z, are identified. We show dependence of the steady state phase diagrams on the collective (nonlocal) dissipation. In Sec. IV, we explore the linear stability of the steady state. Dynamics of different phases, in particular the multistable phases, are discussed. In Sec. V, we numerically obtain the quantum correlation and Von Neumann entropy in the quantum master equation, and link the result with mean-field predictions. We conclude in Sec. VI.

II. THE MODEL

We consider a one-dimensional lattice of N atoms in electronically high-lying Rydberg states $|1\rangle$ and $|2\rangle$, as depicted in Fig. 1. Similar to the experiment [8], we assume that states $|2\rangle = |nD\rangle$ and $|1\rangle = |(n+1)P\rangle$ with n to be the principal quantum number. These states are coupled by a microwave (MW) field with Rabi frequency Ω and detuning Δ. In Rydberg state $|s\rangle$ $(s = 1, 2)$, atoms located at site j and k interact strongly with vdW interactions $V_{jk}^{(s)} = C_6^s/a^6|j-k|^6$ where C_6^s and a are the dispersion coefficient and lattice constant. The interstate interaction is neglected, as the two states are energetically separated [48]. Hamiltonian of the many-body system is given by ($\hbar = 1$) [8]

$$H = \sum_j^N \left[\frac{\Omega}{2}\sigma_x^j - \frac{\Delta}{2}\sigma_z^j\right] + \frac{1}{2}\sum_{\alpha=1,2}\sum_{k\neq j}^N V_{jk}^{(\alpha)}\sigma_{\alpha\alpha}^j\sigma_{\alpha\alpha}^k + \frac{1}{2}\sum_{k\neq j}^N V_{jk}^{DD}\left(\sigma_x^j\sigma_x^k + \sigma_y^j\sigma_y^k\right). \quad (1)$$

where σ_ξ^j $(\xi = x, y, z)$ are the Pauli matrices on site j, $\sigma_{(\pm)}^j = \frac{1}{2}(\sigma_x^j \pm i\sigma_y^j)$ is the raising (lowering) operator, and $\sigma_{ss}^j = [1+(-1)^s\sigma_z^j]/2$ are projection operators to the Rydberg state. The dipole-dipole (DD) interaction is given by $V_{jk}^{DD} = C_3(1-3\cos^2\theta_{jk})/a^3|j-k|^3$, where θ_{jk} is the angle between their internuclear axis and quantization axis.

The Rydberg states are subject to individual and collective (superradiant) decay [8]. Dynamics of the system are governed by the Lindblad master equation [3]

$$\dot{\rho}(t) = -i[H, \rho(t)] + \mathcal{L}[\rho(t)], \quad (2)$$

where ρ is the many-body density matrix, and operator $\mathcal{L}(\rho)$ describes the dissipation,

$$\mathcal{L}[\rho] = \sum_{j,k}^N \frac{\Gamma_{jk}}{2}[2\sigma_-^j\,\rho\,\sigma_+^k - \{\sigma_+^k\sigma_-^j, \rho\}], \quad (3)$$

where Γ_{jk} is the collective decay rate between site j and k. When $j = k$, single-body decay rate $\gamma_s = \Gamma_{jj} = \omega_j^3\mu_j^2/3\pi\epsilon_0\hbar c^3$, where ω_j is the transition frequency and μ_j is the dipole moment [3]. If the atom separation R_{jk} is much larger than the photon wavelength $\lambda = 2\pi c/\omega$, the decay is dominated by the individual (local) ones. For densely packed atoms, superradiance leads to nonlocal dissipation that varies with the distance between atoms [3, 49, 50]. In our analysis, we neglect the distance dependence as the average spacing ($\sim \mu$m) between Rydberg atoms is much smaller than the MW wavelength ($\sim$ mm). In a mesoscopic setting (tens to hundreds of atoms), the collective decay becomes all-to-all with equal strength, i.e. $\Gamma_{jk} = \gamma_m$ [47].

In the following discussions, the DD interaction will be neglected for the following reason. First, in our recent experiment [8] it has been shown that superradiance in dense Rydberg gases is strongly affected by the van der Waals interactions while effects due to the DD interaction is not significant. This is due to the fact that dipolar interactions are long-ranged ($\sim R^{-3}$), but the vdW interaction is short-ranged ($\sim R^{-6}$). The vdW interaction can be stronger than the DD interaction at short distances (see Appendix A for illustrations). Second, one can turn off the DD interaction by adopting the magic angle (i.e., $1 - 3\cos^2\theta_{jk} = 0$) in the one-dimensional model (see Appendix A for details). The influence of the DD interaction on Rydberg superradiant dynamics will be discussed elsewhere.

III. MEAN-FIELD PHASES

The Hilbert space of the Hamiltonian grows as 2^N, while the dimension of the density matrix is 2^{2N}. The computational complexity prevents us from numerically solving the many-body problems when $N > 10$ in typical computers. Due to the dissipation, we could employ the mean-field (MF) theory to analyze the steady state and dynamics. In the MF approximation, the many-body density matrix ρ is decoupled into individual ones through $\hat{\rho} \approx \Pi_i\ \hat{\rho}_i$. This decoupling essentially ignores quantum entanglement between different sites [51]. We obtain MF equations of motion of the spin expectation values [8]

$$\dot{S_x^j} = -\frac{\gamma_s}{2}S_x^j + \Delta S_y^j + \sum_{k\neq j}\left(S_y^j S_V^{jk} + \mathcal{F}_x^{jk}\right), \tag{4a}$$

$$\dot{S_y^j} = -\frac{\gamma_s}{2}S_y^j - \Delta S_x^j - \Omega S_z^j - \sum_{k\neq j}\left(S_x^j S_V^{jk} - \mathcal{F}_y^{jk}\right), \tag{4b}$$

$$\dot{S_z^j} = -\frac{\gamma_s}{2}(1+2S_z^j) + \Omega S_y^j - \gamma_m \sum_{k\neq j}\mathcal{D}^{jk}, \tag{4c}$$

where $S_\xi^j = \frac{1}{2}\mathrm{Tr}(\sigma_\xi^j\hat{\rho})$ are the expectation values of operator σ_ξ^j, $\mathcal{D}^{jk} = S_x^j S_x^k + S_y^j S_y^k$ and $\mathcal{F}_\xi^{jk} = \gamma_m S_z^j S_\xi^k$. We have defined the site-dependent interaction term $S_V^{jk} = [V_{jk}^{(1)}(1-2S_z^k) - V_{jk}^{(2)}(1+2S_z^k)]/4 = [(V_{jk}^{(1)} - V_{jk}^{(2)}) - 2S_z^k(V_{jk}^{(1)} + V_{jk}^{(2)})]/4$, which is dependent on the interaction strength and S_z. It shows that the nonlinear interaction will decrease when $V_{jk}^{(1)} \sim -V_{jk}^{(2)}$. Note that the vdW interaction decreases rapidly with spin separations ($\propto 1/a^6|j-k|^6$). In the coherent regime, the classical groundstate forms crystalline structures in the thermodynamic limit [52–55]. The Rabi coupling, on the other hand, could melt the crystalline phase [56]. The vdW type interaction between Rydberg atoms means that the nearest-neighbor (NN) interaction is p^6 times of other long-range interactions (with atom separation pa with $p \geq 2$). Typically the long-range tail of the vdW interaction leads to subtle details in the crystal melting [57–59]. Following Ref. [47], we will take into account of the NN interaction $V_{1(2)} = C_{1(2)}/a^6$ in the following analysis. Without losing generality, we will scale energy with respect to γ_s in the numerical simulations, except in Sec. IV-C.

At the mean-field level, the nonlocal, collective decay leads to nonlinear dissipative terms in the mean-field equations, while local decay leads to linear dissipative terms (see Eq. (4)). The collective decay is all-to-all and independent of distance. Depending on the parameters, we find Rydberg populations in the MF steady state can have different distributions along the lattice. To characterize the phases, we will use S_z as an order parameter, and identify uniform (UNI), and non-uniform solutions.

A. Uniform phases

The uniform phase corresponds to spatially homogeneous excitation of both Rydberg states. To obtain the uniform solution, one can find the fixed point through

$$\dot{S_x} = -\frac{\gamma_s}{2}S_x + \tilde{\Delta}S_y + \kappa S_z S_x, \tag{5a}$$

$$\dot{S_y} = -\frac{\gamma_s}{2}S_y - \tilde{\Delta}S_x - \Omega S_z + \kappa S_z S_y, \tag{5b}$$

$$\dot{S_z} = -\frac{\gamma_s}{2}(1+2S_z) + \Omega S_y - \kappa\left(S_x^2 + S_y^2\right), \tag{5c}$$

where $\tilde{\Delta} = \Delta + S_V$, and $\kappa = (N-1)\gamma_m$. Order parameter S_z in the UNI phase satisfies

$$\tilde{\Delta}^2 + \left(\frac{\gamma_s}{2} - \kappa S_z\right)^2 + \frac{\Omega^2 S_z}{2S_z+1} = 0. \tag{6}$$

This is a nonlinear function of S_z, where analytical solutions are typically difficult to derive. In a special case, $V_1 = -V_2 = V$, an analytical solution can be obtained. The expression of the solution is lengthy and is given in Appendix B. In general conditions, solutions in the uniform phase are obtained numerically. According to values of Rydberg excitation, we further divide the UNI phase into low-excitation phase (ULE phase) when $-1/2 < S_z < -1/4$ (i.e., the population on level $|2\rangle$ $S_{22} = 0.5 + Sz$; it satisfies $0 < S_{22} < 1/4$), and high-excitation phase (UHE phase) if $-1/4 < S_z < 1/2$ (i.e., $1/4 < S_{22} < 1$).

B. Non-uniform phases

Due to the NN interaction, we employ a bipartite sublattice ansatz to analyze the stationary states. Here two NN sites, labelled with A and B, repeat their pattern periodically throughout the lattice. With this periodicity in mind, Eq. (4) is simplified to the following coupled equations of the $A-B$ sublattice,

$$\dot{S_x^A} = -\frac{\gamma_s}{2}S_x^A + (\Delta + S_V^B)S_y^A + \frac{N\gamma_m\mathcal{C}_x}{2}S_z^A, \tag{7a}$$

$$\dot{S_y^A} = -(\Delta + S_V^B)S_x^A - \frac{\gamma_s}{2}S_y^A + \frac{N\gamma_m\mathcal{C}_y - 2\Omega}{2}S_z^A, \tag{7b}$$

$$\dot{S_z^A} = \Omega S_y^A - \frac{\gamma_s}{2}(1+2S_z^A) - \frac{N-2}{2}\gamma_m(S_\perp^A)^2 - \frac{N\gamma_m}{2}\mathcal{D}^{AB}, \tag{7c}$$

with $S_\perp^\alpha = \sqrt{S_x^{\alpha\,2} + S_y^{\alpha\,2}}$ ($\alpha = A, B$) is the projection of α-spin on the $x-y$ plane and $\mathcal{C}_\xi = (N-2)S_\xi^A/N + S_\xi^B$. Equations for B sites can be obtained by swapping index A and B in Eq. (7). We then obtain MF steady state solutions by solving these equations numerically.

According to values of S_z^α, we identify antiferromagnetic (AFM), oscillatory (OSC) phase, and bistable/multistable phases. In AFM phases one sublattice has a higher excitation than the other ($S_z^A \neq S_z^B$).

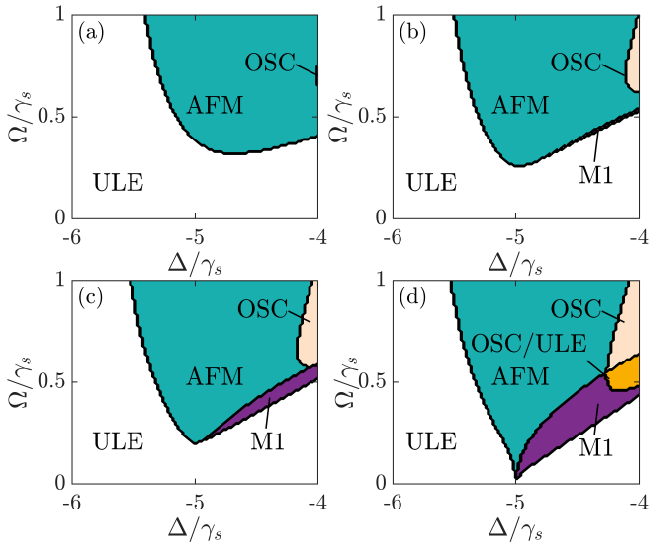

Figure 2. Mean-field phase diagrams for (a) $\gamma_m = 0$, (b) $\gamma_m = 0.6$, (c) $\gamma_m = 0.8$, and (d) $\gamma_m = 1$. When γ_m is small, the phase diagram is mainly occupied by the UNI phase (ULE and UHE), AFM phase, and OSC phase. When γ_m is large, bistable (OSC/ULE with orange area) and multistable phases (M1 with purple area) can be seen in panels (b), (c), and (d). Other parameters are $V_1 = 10$, $V_2 = 10$, and $\gamma_s = 1$.

The AFM phase is stationary, which means that S_z^α will not change with time when $t \to +\infty$. In the OSC phase, however, populations of two neighboring sites oscillate over time.

C. Phase diagrams

Examples of MF phase diagrams for different values of γ_m are shown in Fig. 2. They elaborate on the consequences arising from the nonlocal character of the dissipation. Without the nonlocal decay ($\gamma_m = 0$) (Fig. 2(a)), the steady state is dominated by a ULE phase when Ω is small and $\Delta < 0$. By decreasing $|\Delta|$ and increasing Ω, the ULE phase becomes unstable and enters into the AFM phase, due to the competition between the local decay and vdW interaction [47]. It is found that the OSC phase emerges when roughly $\Omega > 0.6$ and $\Delta > -4$. More details on the phases without superradiance can be found in Appendix C. The presence of the Rydberg superradiance enhances the nonuniform phase and also brings multistable phases. As shown in Fig. 2(b)-(c), areas of the ULE phase shrink when increasing γ_m, while areas of the nonuniform phase, especially the OSC phase, increase drastically. Importantly, a new *multistable* phase (labeled by M1) emerges in which the AFM, OSC, and ULE phases coexist. For example, we find both a bistable region of the OSC and ULE phase, and a M1 phase when $\gamma_m = \gamma_s$, as depicted in Fig. 2(d).

The rich MF phases result from the competition between the collective decay and strong vdW interaction.

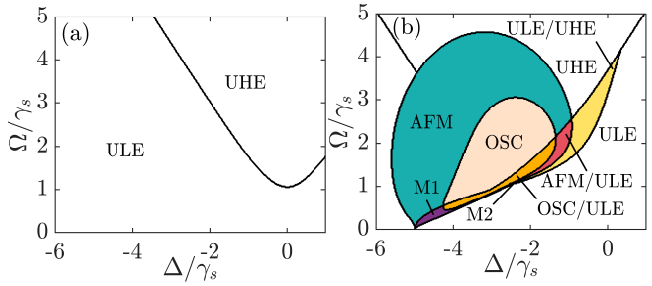

Figure 3. Homogeneous phases when (a) $V_1 = V_2 = 0$ and more structured phases when (b) $V_1 = V_2 = 10$. These figures show that the strong vdW interactions turn the simple uniform phase into complicated phases. Parameters are $\gamma_s = \gamma_m = \gamma = 1$.

Without the vdW interaction, we only find uniform phases, as shown in Fig. 3(a). Here the ULE phase smoothly crosses over into the UHE phase as Ω is increased while Δ is fixed. When $V_1 = V_2 = 10$, on the other hand, a variety of nonuniform phases are generated, as shown in Fig. 3(b). Here even in the UNI phase, we find a bistability between the ULE/UHE phases when $|\Delta| \sim 0$. Note the bistable ULE/UHE phase is different from the AFM phase in that the population in the $A-B$ site is still same in the former case. The transition to these steady phases depends on initial conditions [40, 50], which will be demonstrated in detail in the next section. Other bistable phases, including AFM/ULE and OSC/ULE phases, are also found, though they occupy a small parameter space. We also find a new multistable phase in which AFM(OSC)/ULE/UHE solutions (labeled by M2; see Fig. 4(a1) below for detail) are found. This multistable phase can only occupy a very small region in the parameter space. Hence the vdW interaction and nonlocal dissipation between different atoms together result to complicated phases [50]. In the following, we will focus on the bistable and the multistable M2 phases.

IV. STABILITY AND DYNAMICS OF THE MEAN-FIELD PHASES

The phase diagram obtained previously is based on mean-field calculations with Eq. (6) (uniform phases) and Eq. (7) (bistable and multistable phases). In the following, we will study stabilities of these phases in a long chain $N \gg 2$, and hence verify especially the stability of the M1 phase.

A. Linear stability analysis

We first present examples of the multistability and bistability as a function of Ω in Fig. 4(a1). The blue lines represent the uniform solutions and the orange lines

represent the nonuniform solutions. We then analyze the linear stability of the steady state solution by calculating eigenvalues λ_j of the Jacobian matrix of Eqns. (7) [60]. If the real parts of all eigenvalues are negative, i.e. $\mathrm{Re}(\lambda_j) < 0$, the corresponding solution is stable (solid lines); otherwise, it is unstable (dotted lines).

When Ω is small, the steady state is the ULE phase, then changes to the OSC/ULE phase and then to the M1 phase by increasing Ω (Fig. 4(a1)). The nonuniform fix points become stable which means the system shows an antiferromagnetic pattern. These unstable nonuniform fixed points lead to the OSC phase, in which the Rydberg population oscillates periodically in time. In particular we find multistable solutions in the M1 phase (AFM/OSC/ULE), ULE solutions are stable while two other solutions are not stable. Further increasing Ω, the nonuniform solutions become unstable while the UHE phase becomes stable at a critical Ω_c (marked by C) after passing through the very narrow M2 phase and the ULE/UHE phase.

B. Dynamics of the multistable phase

In the multistable phase, atoms at different sites can occupy different stable populations. To verify this, we solve Eq. (4) numerically with $N = 50$ and periodic boundary conditions. The initial values of different atoms are $\{S_x^i, S_y^i, S_z^i\} = \{0, 0, r\}$, where r is a random number between -0.5 and 0.5. We then probe the multistable phase by tuning the parameters. In Fig. 4(b1) and (b2), we show mean values of S_z^j for a block of 6 sites with index $j = 1 \sim 6$. As shown in Fig. 4(a1), the simple two-site MF theory predicts three stable solutions in the M1 phase, which can be seen in the dynamical simulation with $N = 50$. We note that in the many site simulation, the system prefers a ULE and OSC solution when Ω is approaching to the lower critical value around 5.8, as the example shown in Fig. 4(b1). Increasing Ω, the three phases coexist in the dynamical simulation, as shown in Fig. 4(b2). The OSC phase oscillates around the AFM phase and its oscillation amplitude reduces with the Rabi frequency. Further increasing Ω, the strength of the OSC phase gradually reduces such that only the AFM and ULE phase survive.

To characterize distributions of the Rydberg spin population across the lattice, we evaluate the variance σ of the spins in different sites [50]

$$\sigma = \frac{1}{N}\sum_i^N (\bar{\mathbf{S}} - \mathbf{S}^i)^2, \tag{8}$$

where $\mathbf{S}^i = (S_x^i, S_y^i, S_z^i)/S, S = \sqrt{(S_x^i)^2 + (S_y^i)^2 + (S_z^i)^2}$, and $\bar{\mathbf{S}} = \sum_j^N \mathbf{S}^j/N$ is the average spin. Here the translational symmetry of the lattice is broken when $\sigma \neq 0$, which takes place, for example, in the AFM phase [47]. In Fig. 4(a2), we show the variance obtained from a simulation by varying Ω. The spin fluctuations are large

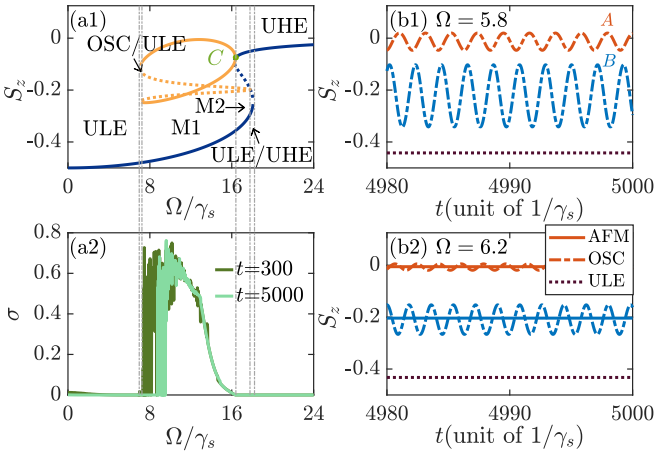

Figure 4. Superradiance dependent multistability. When increasing Ω, a series of phase transitions can be found in (a1). The solid (dotted) lines correspond to the stable (unstable) solutions. The blue (orange) lines correspond to the uniform (nonuniform) solutions. Multiple solutions coexist to represent the multistable phase. Point C is the critical point between the nonuniform and UHE phase. The grey dash lines indicate the crossing into OSC/ULE, M1, M2, ULE/UHE, and UHE regions, respectively. Dynamics of Rydberg populations in the (b1) M1 phase with $\Omega = 5.8$ and (b2) M1 phase with $\Omega = 6.2$. Different curves represent different simulations. The red (blue) lines denote the dynamical behaviors of atoms in site A (B) of the simulation. The solid lines correspond to the AFM phase, the dash lines correspond to the OSC phase, and the dotted lines correspond to the ULE phase. (a2) Variance σ as a function of Rabi frequency in the long-time limit $t = 300$ and $t = 5000$. Other parameters are $N = 50$, $\Delta = -2$, $V_1 = V_2 = 10$, and $\gamma_s = \gamma_m = 0.5$.

especially in the M1 phase due to different sites occupying very different populations. In the M1 phase, we find the variance reaches maximal values when the OSC phase dominates. It decreases when increasing Ω, as the strength of the OSC phase decreases, while the AFM and ULE phase become important. We have evaluate the values at two different times. It is found that the spin fluctuation persists even when $t = 5000$, indicating that the various phases are truly stable. Note that in the bistable phases, the atoms will pick up either the lower or the upper branch of the solution in individual simulations, hence $\sigma = 0$ in these phases.

C. The critical value Ω_c

As shown in Fig. 4(a1), point C marks the boundary between the M1 and UHE phase. It is interesting to understand the critical value Ω_c that distinguishes these two phases. When increasing $\gamma_s = \gamma_m = \gamma$, our numerical simulations indicate that Ω_c increases, as shown in Fig. 5(a). In addition, the critical value increases with N monotonically for a given γ, as the effective collective decay rate of each atom is proportional to $(N-1)\gamma_m$.

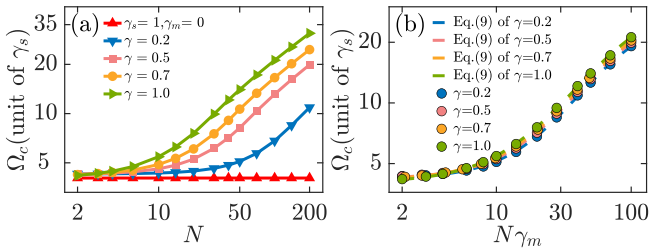

Figure 5. Scaling of the critical value Ω_c with respect to (a) atom numbers N and (b) parameter $N\gamma_m$ for different γ. (b) The colored dots denote numerical simulation, and the lines represent analytical results from Eq. (9).

Note that Ω_c can only be tuned in the superradiance regime. When $\gamma_m = 0$, it will be a constant and has no dependence on N any more.

As shown in Fig. 5(a), Ω_c increases nearly linearly when N and γ_m are large, which displays different scaling when N and γ_m are small. To understand this behavior, one notes that the critical point can be obtained by solving Eq. (7). Approaching the critical point from the UHE phase, S_z is solved numerically using Eq. (6). We derive an analytical solution,

$$\Omega_c = \sqrt{-\frac{2S_z+1}{S_z}\left[(\Delta+S_V)^2+\left(\frac{\gamma_s}{2}-(N-1)\gamma_m S_z\right)^2\right]}. \tag{9}$$

The analytical Ω_c shows that the critical point will depend on N if $\gamma_m \neq 0$. When $N\gamma_m < \gamma_s$, Ω_c varies with S_V and γ_s nonlinearly. Hence this is a regime where the vdW interaction dominates, as S_V is affected by the vdW interaction. When $N\gamma_m$ is large, on the other hand, one can expand Ω_c by assuming γ_s and S_V small, leading to $\Omega_c \sim \sqrt{-S_z(2S_z+1)}(N-1)\gamma_m$. In Fig. 5(b), the scaled Ω_c with respect to $N\gamma_m$ are shown. The numerical data agree with the analytical prediction Ω_c well.

V. QUANTUM MANY-BODY DYNAMICS OF FINITE 1D CHAINS

MF theory is expected to be valid in higher dimensions where quantum fluctuations are averaged out. Despite this, MF theory can capture qualitative aspects of the quantum system. To illustrate signatures of the MF phases, we numerically solve the master equation (2) for a 1D chain of length $N = 8$ with periodic boundary conditions in the long-time limit $t = 300$. In Fig. 6(a) and (b), mean values of spin population, $\langle\sigma_z\rangle = 1/N\sum_j \mathrm{Tr}(\rho_s\sigma_z^j)$, in the stationary state ρ_s are shown. It is found that some trends of the master equation calculation agree with the MF prediction. For example, in the M1 (Fig. 6(a) and (b)), mean values of the spin component σ_z becomes large when varying Δ or Ω. This means spin state $|2\rangle$ is excited in these parameter regions. A consequence is that the von Neumann entropy $\mathcal{S} = -\mathrm{Tr}(\rho_s \ln \rho_s)$ in the

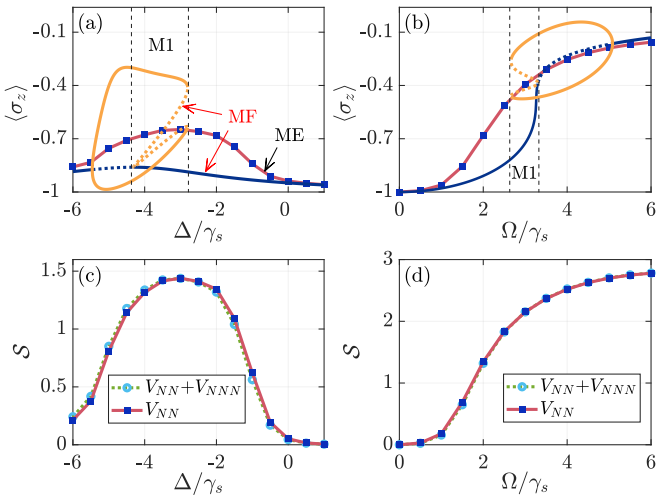

Figure 6. Numerical solutions of the master equation (ME) and MF calculations for 1D chain of length $N = 8$ with periodic boundary conditions. Mean population $\langle\sigma_z\rangle$ by varying (a) detuning Δ with $\Omega = 2$ and (b) Rabi frequency Ω for $\Delta = -2$. The red lines represent the master equation results. The blue and orange curves are MF results. The M1 phase is highlighted in (a) and (b). The tendency of the MF and master equation calculation is similar. It seems that the M1 phase emerges before $\langle\sigma_z\rangle$ reaches the maximal value when increasing Δ or Ω. The respective Von Neumann entropy in panel (c) and (d) has similar shapes as that of $\langle\sigma_z\rangle$ shown in (a) and (b). The dark blue squares are calculated by only considering the NN interaction (V_{NN}) while the light blue circles by considering both NN and the next NN interaction (V_{NN} and V_{NNN}). Other parameters are $N = 8$, $\gamma = 1$, $V_1 = 5$, and $V_2 = 5$.

steady state also becomes large (Fig. 6(c) and (d)). As shown in Fig. 6(c) and (d), even longer range interactions (i.e. next nearest-neighbor interactions) only plays a minor role, justifying that it is a good approximation to consider only the nearest-neighbor interaction in the calculation.

Another important quantity is the correlation between different lattice sites, $\langle\sigma_z^i\sigma_z^{i+j}\rangle_c = \langle\sigma_z^i\sigma_z^{i+j}\rangle - \langle\sigma_z^i\rangle\langle\sigma_z^{i+j}\rangle$ [47]. Due to a periodic boundary condition, the correlation will vary with the lattice separation. For concreteness, we consider $i = 1$ and $0 \leq j \leq 8$ in the calculation. The correlation exhibits rather different features in different MF phases. In the ULE phase, the correlation decays rapidly with increasing distance and vanishes when $j > 1$, which is independent of γ_m, shown in Fig. 7(a). In the ULE phase, atoms in the system are largely in the low-lying $|1\rangle$ state. Hence jumping from state $|2\rangle$ to $|1\rangle$ is unlikely, such that the stationary state as well as the correlation is largely insensitive to γ_m. This, however, changes in the UHE phase, where the occupation in state $|2\rangle$ in every site is large. In this phase, the superradiance plays an important role in the stationary state. As shown in Fig. 7(b), a long-range, positive correlation is obtained when $\gamma_m = 1$, while the correla-

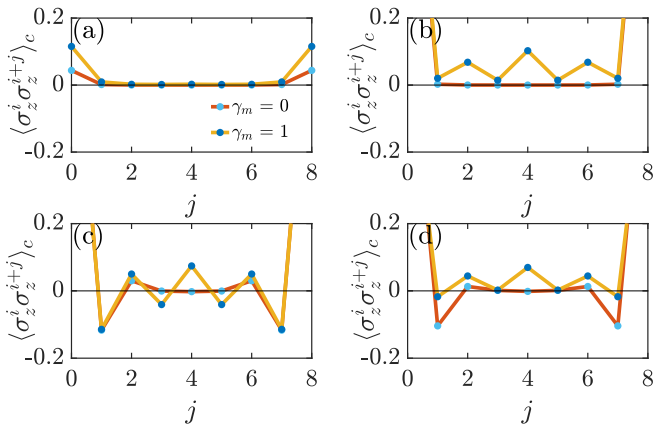

Figure 7. The correlation operator $\langle \sigma_z^i \sigma_z^{i+j} \rangle_c$ as a function of distance with $\gamma_s = 1$, $V_1 = V_2 = 5$ for $N = 8$ spins on a chain with periodic boundary conditions. (a) ULE phase $\Delta = 0$, $\Omega = 2$, (b) UHE phase $\Delta = 0$, $\Omega = 8$, (c) AFM phase $\Delta = -3$, $\Omega = 4$, (d) OSC (M1) phase $\Delta = -3, \Omega = 2.4$ for $\gamma_m = 0(1)$.

tion does not exist any more when $\gamma_m = 0$. In the AFM phase (Fig. 7(c)), we find that the correlation oscillates between positive and negative values with increasing j when $\gamma_m = 1$. In the M1 phase region, however, the correlation is negative when $j = 1, 7$, and becomes positive at large separations (Fig. 7(d)). The correlation, however, decays with increasing separation when $\gamma_m = 0$. This indicates that the nonlocal decay can enhance the two-body correlation. Hence the different profiles of the spin-spin correlation could be used to characterize the MF phases.

VI. CONCLUSIONS

We have investigated stationary phases of a 1D chain of MW coupled, strongly interacting Rydberg atoms with nonlocal dissipations. Using MF theory, we have obtained interesting bistable and multistable solutions in the stationary state. By analyzing the MF phase diagram, the dependence of the multistable phases on the MW coupling, nonlocal dissipation as well as vdW interaction is studied. Dynamical simulations show that Rydberg atoms in different sites occupy all available solutions simultaneously in the multistable phase. We have found the critical value Ω_c between the multistable and UHE phase. The scaling of Ω_c is examined, and agrees with numerical calculations. By solving the master equation numerically for a finite chain, it is found that certain features predicted by the MF theory persist in the quantum regime. Different profiles of the spin-spin correlation could be used to probe and characterize the MF phases. Such superradiance induced many-body phase transition is observable with current experimental condition[8, 61]. Our study is relevant to current theoretical [62] and experimental [8] efforts in understanding and probing dynamics due to the interplay between strong vdW interactions and superradiant decay in arrays of Rydberg atoms.

ACKNOWLEDGMENTS

Y. H., Y. J., and J. Z. are supported by the National Natural Science Foundation of China (Grant No. 12120101004, 61835007, 62175136); the Scientific Cooperation Exchanges Project of Shanxi province (Grant No. 202104041101015); Changjiang Scholars and Innovative Research Team in Universities of the Ministry of Education of China (IRT 17R70); the Fund for Shanxi 1331 Project. Z. B. acknowledge National Natural Science Foundation of China (11904104, 12274131), and the Shanghai Pujiang Program under grant No. 21PJ1402500. W. L. acknowledges support from the EPSRC through Grant No. EP/W015641/1.

Appendix A: Dipole-dipole and vdW interactions

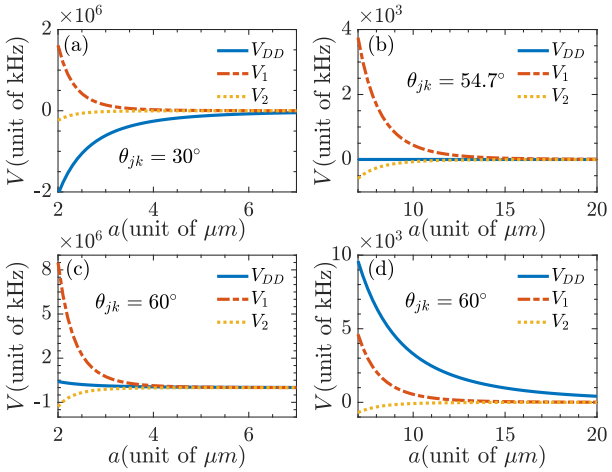

Figure A1. DD and vdW interactions. In (a) $\theta_{jk} = 30°$, where the vdW interaction is comparable to the DD interaction. In (b) $\theta = 54.7°$, the DD interaction is zero. In (c) and (d), $\theta_{jk} = 60°$. We can see that the vdW interaction is important at short distances (c), while the DD dominates when atom separations are large (d).

In this section, we discuss the strength of both DD and vdW interactions and the motivation of neglecting the DD interaction in this work. The experimental and numerical results in our recent work [8] demonstrate that the dipolar interaction effect might not be critical in dense gas. This is because that dipolar interactions are a long-range interaction ($\sim R^{-3}$), but the van der Waals interaction is short-ranged ($\sim R^{-6}$). For high atomic density, the distance between atoms is small ($R \leq \lambda$), where the vdW interaction could play a dominant role (see Fig. A1 for illustrations). Moreover, we can control the strength of the DD interaction by manipulating the

angle θ_{jk}. To highlight the contribution of vdW interaction in one-dimensional system, we can adjust the magic angle $(1-3\cos^2\theta_{jk}=0)$ to turn off the DD interaction. Hence the DD interactions can be safely ignored in our model (see blue line in Fig. A2).

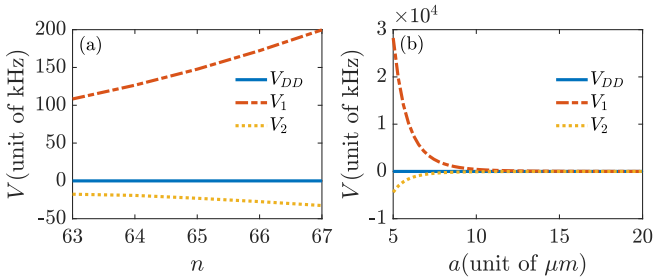

Figure A2. (a) The interaction energy (including DD and vdW interactions) as a function of the principal quantum number n with lattice constant $a = 12\mu m$. (b) The interaction energy varies with lattice spacing a when $n = 65$. Here we select the magic angle where $\theta_{jk} = \arccos(\frac{1}{\sqrt{3}}) \approx 54.7°$, the dipole-dipole interaction V_{DD} is close to zero.

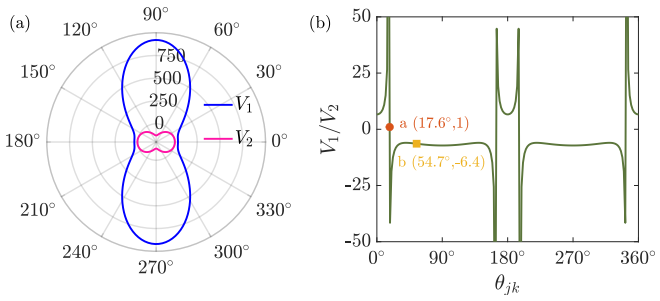

Figure A3. The calculation results with experimental parameters. (a) The dispersion coefficient C_6 varies with angular θ_{jk} . (b) The ratio between V_1 and V_2 as a function of θ_{jk}. The point a and b indicates $V_1 = V_2$ [the corresponding MF phase diagram is shown in Fig. 3(b)] and $V_1 = -6.4V_2$ [the corresponding MF phase diagram is shown in Fig. A4], respectively.

In this work cesium atoms are used with $|1\rangle = |(n+1)P_{3/2}\rangle$ and $|2\rangle = |nD_{5/2}\rangle$. The dispersion coefficient C_6 can be calculated using ARC package [63]. The results shows that dispersion coefficients in states $|(n+1)P_{3/2}\rangle$ and $|nD_{5/2}\rangle$ are both anisotropic [see Fig. A3(a)]. From Fig. A3(b), one can see that the ratio between V_1 and V_2 can be precisely controlled by manipulating the angle θ_{jk}. The condition for $V_1 = V_2$ is achievable in our system when $\theta_{jk} \approx 17.6°$ [see point a in Fig. A3(b)]. We also conduct the simulation at the magical angle with interaction strength $V_1 = 32$, $V_2 = -5$ [correspond to point b in Fig. A3(b)]. Their corresponding MF phase diagram is shown in Fig. A4. Similar to the result given in Fig. 3(b) in the main text, abundant many-body phases can also be obtained here.

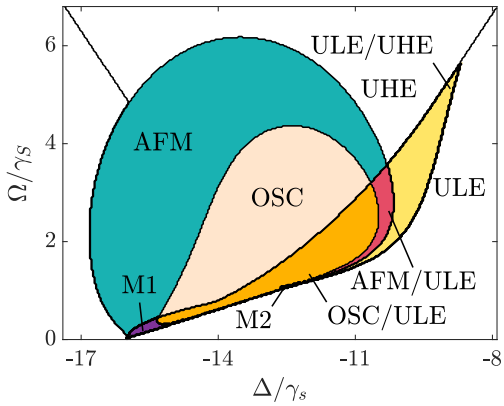

Figure A4. MF phase diagram with $V_1 = 32$ and $V_2 = -5$. The superradiance rate is used with $\gamma_s = \gamma_m = 1$.

Appendix B: Analytical Solutions of the uniform phase

When $V_1 = -V_2 = V$, $\tilde{\Delta} = \Delta + V/2$, we can obtain the uniform solutions analytically,

$$S_z = \frac{1}{12\kappa}\left\{-2\kappa + 4\gamma_s + \frac{4(\Gamma^2 - 6c_1)}{(\sqrt{3}i-1)c_3^{\frac{1}{3}}} + (\sqrt{3}i-1)c_3^{\frac{1}{3}}\right\} \tag{B1}$$

where we have defined parameters,

$$\begin{aligned}
\Gamma =& \kappa + \gamma_s,\\
c_1 =& 2\tilde{\Delta}^2 + \Omega^2,\\
c_2 =& (-\Gamma^2 + 6c_1)^3 + [\Gamma^3 + 36\Gamma\tilde{\Delta}^2 - 9(\kappa - 2\gamma_s)\Omega^2]^2,\\
c_3 =& -\kappa^3 - 3\gamma_s\kappa^2 - 3[\gamma_s^2 + 3(4\tilde{\Delta}^2 - \Omega^2)]\kappa - \gamma_s(\gamma_s^2\\
&+ 18c_1) + \sqrt{c_2}.
\end{aligned}$$

This expression is lengthy and therefore is not shown in the main text. It agrees with the numerical simulation.

Appendix C: MF Phases without Superradiance

The mean-field phase diagram without superradiance is shown in Fig. A5. Similar work has been studied in Ref. [40]. The difference is that the two-level system in our model consists of two Rydberg states. Compared to the superradiance phase diagram (see Fig. 3(b) in the main text), the influence of superradiance is negligible when the MW field driving is strong. Around $-5 < \Delta < -1$, superradiance makes obvious changes. For example, the stable ULE phase in Fig. A5 becomes nonuniform and emerges M1 phase.

We further study the influence of vdW interaction on phase transitions. Fig. A6 shows the mean-field phase diagrams as a function of Δ and V_1 for $\Omega = 2$ with the vdW interaction V_2 is equal to 0, 5, 10, respectively. Fig. A6(a) shows the phase is symmetric with respect to the origin,

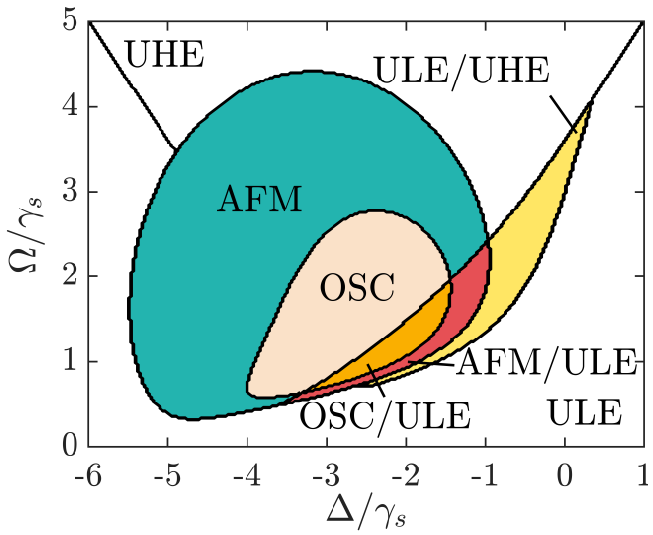

Figure A5. Mean-field phase diagram without superradiance. Other parameters are $V_1 = 10$ and $V_2 = 10$.

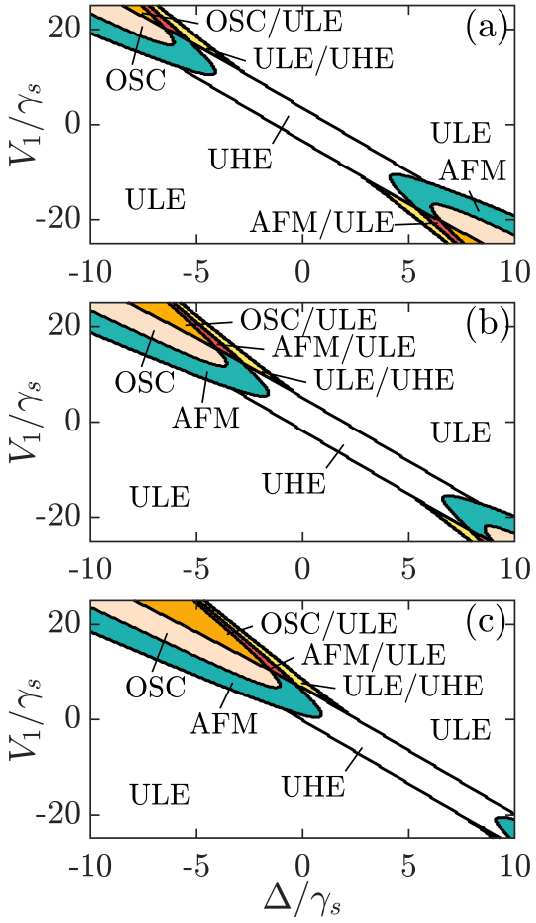

Figure A6. Mean-field phase diagrams for different V_2. (a) $V_2 = 0$, (b) $V_2 = 5$, (c) $V_2 = 10$. The interaction V_2 acts as a detuning shift in the phase space. Here $\Omega = 2$.

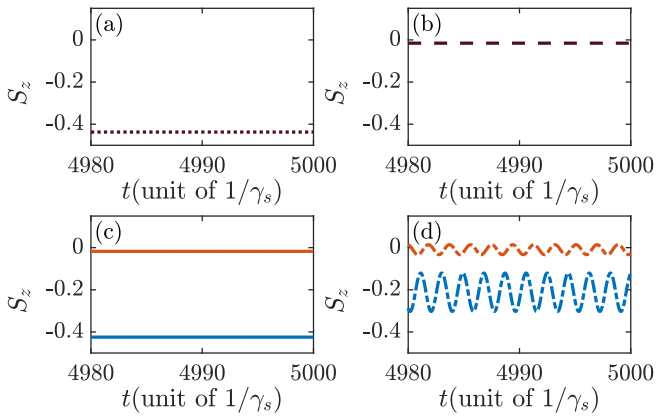

Figure A7. Dynamics of the order parameter S_z^j ($j = 1 \sim 6$) with different interaction and $N = 50$, $\Delta = -2$, $\Omega = 6$, $\gamma = 0.5$, (a) ULE phase with $V_1 = 0$, $V_2 = 5$, (b) UHE phase with $V_1 = 0$, $V_2 = -5$, (c) AFM phase with $V_1 = 2.5$, $V_2 = 5$, (d) OSC phase with $V_1 = 5$, $V_2 = 5$. The purple dotted lines correspond to the UNI phase. The red (blue) lines denote the dynamical behaviors of atoms in site A (B) at the same simulation. The solid lines correspond to the AFM phase, the dash lines correspond to the OSC phase.

i. e. one always observes an identical phase at points (Δ,V_1) and (-Δ, -V_1). The central region of the phase diagram is affected by the driving field, i.e. sufficiently strong driving strength changes the system to the UHE phase. When the vdW interaction of the $|1\rangle$ state is weak, $|V_1| < 10$, there is only the UNI phase when scanning the detuning. As the detuning increases, a continuous phase transition occurs from the UHE phase to the ULE phase which means the atoms from the high-lying Rydberg state return to the lower-lying Rydberg state. For positive detuning and negative interaction V_1 which appears as an attractive potential, the uniform phase disappears, and the AFM phase emerges. With the further increase of the parameters, the AFM phase becomes unstable and develops into the OSC phase. A series of continuous phase transitions occur as the interaction V_2 increases. The increase of V_2 breaks the symmetry of the phase diagram and the symmetry point moves downward. The regions of the five phases except the UNI phase increase at positive interaction V_1.

Appendix D: More Examples of Population Dynamics in the MF regime

We simulate the dynamic evolution process to get some insight into the characteristics of different phases with nonlocal dissipation. Fig. A7 shows the dynamics of the first six sites ($N = 50$) with different initial states in the long-time limit around $t = 5000$. Fig. A7(a) shows when $V_1 = 0$, $V_2 = 5$, the spins with different initial states evolve through time to reach the same steady state at the long-time limit. The atoms are almost in the lower

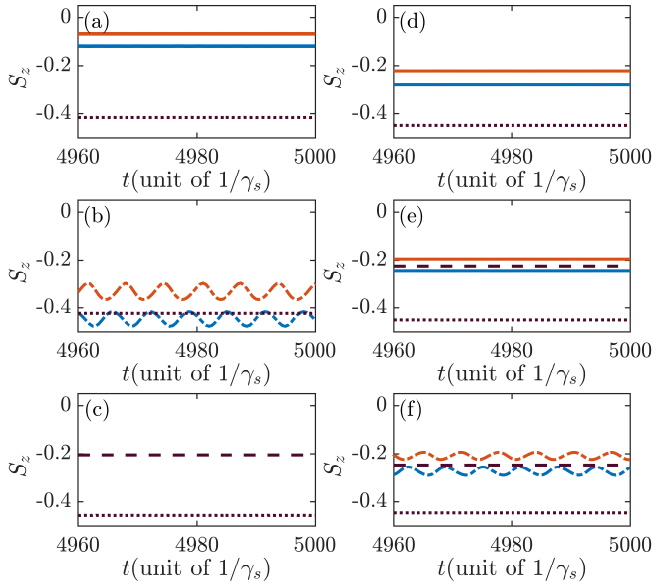

Figure A8. Dynamics for the bistable/multistable phases with the same parameters as in Fig. 3(b). (a) AFM/ULE phase with $\Delta = -1.15$, $\Omega = 2$, (b) OSC/ULE phase with $\Delta = -4.14$, $\Omega = 0.56$, (c) ULE/UHE phase with $\Delta = -0.5$, $\Omega = 2.5$, (d) M1 phase with $\Delta = -2.6$, $\Omega = 1.01$, (e) AFM/OSC/ULE/UHE phase with $\Delta = -2.28$, $\Omega = 1.14$, (f) OSC/ULE/UHE phase with $\Delta = -2.51$, $\Omega = 1.07$.

state, which is in the ULE phase. Fig. A7(b) shows the negative interaction $V_2 = -5$ drives the atoms from the lower state into the superposition state, which dynamics show ULE phase become UHE phase. Fig. A7(a), (c) and (d) have the same parameters but different interaction V_1. With the increase of the interaction V_1, the uniform phase gradually becomes nonuniform and enters the AFM phase. For the AFM phase, the system coexists in two stable steady states that evolve over time in which one has a higher population than the other. Fig. A7(d) shows the population in the OSC phase oscillates periodically in time as V_1 further increase.

For a single simulation, we typically obtain one phase. The bistable and multistable phases are found in different simulations. We consider different initial states to check for bistability. Fig. A8 shows examples of spin dynamics corresponding to the bistable and multistable phase regions in Fig. 3(b). The left panel represents the bistable phases and the right panel represents the multistable phases. In the bistable phase, both phases can coexist. The M2 phase show the existence of AFM and OSC phase (see Fig. A8(e) and (f)).

As N increases, only ULE/UHE phase stability exists. In the bistable ULE/UHE phase, on the other hand, all sites will have identical occupation, and hence all curves collapse to a single line. However, they could have either low occupation or high occupation, depending on the initial condition. In Fig. A9, we have shown two examples from different simulations where all sites have higher (lower) occupations, illustrating the bistable phase.

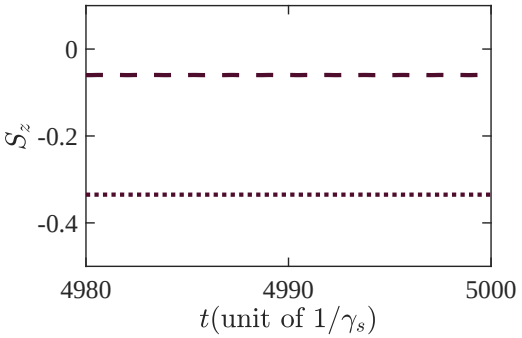

Figure A9. Dynamics simulations of the M2 phase. When $N = 50$, only ULE/UHE phase exists. Different lines represent different simulations. Other Parameters: $V_1 = V_2 = 5$, $\Delta = -2$, $\gamma_s = \gamma_m = 0.5$.

[1] M. Gross and S. Haroche, "Superradiance: An essay on the theory of collective spontaneous emission," Phys. Rep. **93**, 301 (1982).

[2] Robert H Dicke, "Coherence in spontaneous radiation processes," Phys. Rev. **93**, 99 (1954).

[3] Z. Ficek and Ryszard Tanaś, "Entangled states and collective nonclassical effects in two-atom systems," Phys. Rep. **372**, 369–443 (2002).

[4] M Gross, P Goy, C Fabre, S Haroche, and J. M. Raimond, "Maser oscillation and microwave superradiance in small systems of Rydberg atoms," Phys. Rev. Lett. **43**, 343–346 (1979).

[5] L. Moi, P. Goy, M. Gross, J. M. Raimond, C. Fabre, and S. Haroche, "Rydberg-atom masers. I. A theoretical and experimental study of super-radiant systems in the millimeter-wave domain," Phys. Rev. A **27**, 2043–2064 (1983).

[6] T Wang, S. F. Yelin, R Côté, E. E. Eyler, S. M. Farooqi, P. L. Gould, M Koštrun, D Tong, and D Vrinceanu, "Superradiance in ultracold Rydberg gases," Phys. Rev. A **75**, 033802 (2007).

[7] David D. Grimes, Stephen L. Coy, Timothy J. Barnum, Yan Zhou, Susanne F. Yelin, and Robert W. Field, "Direct single-shot observation of millimeter-wave superradiance in Rydberg-Rydberg transitions," Phys. Rev. A **95**, 043818 (2017).

[8] Liping Hao, Zhengyang Bai, Jingxu Bai, Suying Bai, Yuechun Jiao, Guoxiang Huang, Jianming Zhao, Weibin Li, and Suotang Jia, "Observation of blackbody radiation enhanced superradiance in ultracold Rydberg gases," New J. Phys. **23**, 083017 (2021).

[9] Y. Kaluzny, P. Goy, M. Gross, J. M. Raimond, and S. Haroche, "Observation of Self-Induced Rabi Oscillations in Two-Level Atoms Excited Inside a Resonant

Cavity: The Ringing Regime of Superradiance," Phys. Rev. Lett. **51**, 1175–1178 (1983).
[10] Jonas A. Mlynek, Abdufarrukh A. Abdumalikov, Christopher Eichler, and Andreas Wallraff, "Observation of Dicke superradiance for two artificial atoms in a cavity with high decay rate," Nat. Commun. **5**, 5186 (2014).
[11] Elmer Suarez, Philip Wolf, Patrizia Weiss, and Sebastian Slama, "Superradiance decoherence caused by long-range Rydberg-atom pair interactions," Phys. Rev. A **105**, L041302 (2022).
[12] S. Inouye, A. P. Chikkatur, D. M. Stamper-Kurn, J. Stenger, D. E. Pritchard, and W. Ketterle, "Superradiant Rayleigh scattering from a Bose-Einstein Condensate," Science **285**, 571–574 (1999).
[13] Axel U.J. Lode and Christoph Bruder, "Fragmented Superradiance of a Bose-Einstein Condensate in an Optical Cavity," Phys. Rev. Lett. **118**, 013603 (2017).
[14] Liangchao Chen, Pengjun Wang, Zengming Meng, Lianghui Huang, Han Cai, Da-Wei Wang, Shi-Yao Zhu, and Jing Zhang, "Experimental observation of one-dimensional superradiance lattices in ultracold atoms," Phys. Rev. Lett. **120**, 193601 (2018).
[15] Michael Scheibner, Thomas Schmidt, Lukas Worschech, Alfred Forchel, Gerd Bacher, Thorsten Passow, and Detlef Hommel, "Superradiance of quantum dots," Nat. Phys. **3**, 106–110 (2007).
[16] Da-Wei Wang and Marlan O. Scully, "Heisenberg Limit Superradiant Superresolving Metrology," Phys. Rev. Lett. **113**, 083601 (2014).
[17] Wen-Te Liao and Sven Ahrens, "Gravitational and relativistic deflection of X-ray superradiance," Nat. Photonics **9**, 169–173 (2015).
[18] Fritz Haake, Mikhail I. Kolobov, Claude Fabre, Elisabeth Giacobino, and Serge Reynaud, "Superradiant laser," Phys. Rev. Lett. **71**, 995–998 (1993).
[19] Justin G. Bohnet, Zilong Chen, Joshua M. Weiner, Dominic Meiser, Murray J. Holland, and James K. Thompson, "A steady-state superradiant laser with less than one intracavity photon," Nature **484**, 78–81 (2012).
[20] Matthew A. Norcia and James K. Thompson, "Cold-Strontium Laser in the Superradiant Crossover Regime," Phys. Rev. X **6**, 011025 (2016).
[21] Matthew A. Norcia, Matthew N. Winchester, Julia R. K. Cline, and James K. Thompson, "Superradiance on the millihertz linewidth strontium clock transition," Sci. Adv. **2**, e1601231 (2016).
[22] Thomas F. Gallagher, *Rydberg Atoms*, Cambridge Monographs on Atomic, Molecular and Chemical Physics (Cambridge University Press, Cambridge, 1994).
[23] Antoine Browaeys and Thierry Lahaye, "Many-body physics with individually controlled Rydberg atoms," Nat. Phys. **16**, 132–142 (2020).
[24] Pascal Scholl, Michael Schuler, Hannah J. Williams, Alexander A. Eberharter, Daniel Barredo, Kai-Niklas Schymik, Vincent Lienhard, Louis-Paul Henry, Thomas C. Lang, Thierry Lahaye, Andreas M. Läuchli, and Antoine Browaeys, "Quantum simulation of 2D antiferromagnets with hundreds of Rydberg atoms," Nature **595**, 233–238 (2021).
[25] Sepehr Ebadi, Tout T. Wang, Harry Levine, Alexander Keesling, Giulia Semeghini, Ahmed Omran, Dolev Bluvstein, Rhine Samajdar, Hannes Pichler, Wen Wei Ho, Soonwon Choi, Subir Sachdev, Markus Greiner, Vladan Vuletić, and Mikhail D. Lukin, "Quantum phases of matter on a 256-atom programmable quantum simulator," Nature **595**, 227–232 (2021).
[26] Hendrik Weimer, Robert Löw, Tilman Pfau, and Hans Peter Büchler, "Quantum Critical Behavior in Strongly Interacting Rydberg Gases," Phys. Rev. Lett **101**, 250601 (2008).
[27] Igor Lesanovsky and Juan P. Garrahan, "Kinetic Constraints, Hierarchical Relaxation, and Onset of Glassiness in Strongly Interacting and Dissipative Rydberg Gases," Phys. Rev. Lett. **111**, 215305 (2013).
[28] Matteo Marcuzzi, Emanuele Levi, Sebastian Diehl, Juan P. Garrahan, and Igor Lesanovsky, "Universal Nonequilibrium Properties of Dissipative Rydberg Gases," Phys. Rev. Lett. **113**, 210401 (2014).
[29] N. Malossi, M. M. Valado, S. Scotto, P. Huillery, P. Pillet, D. Ciampini, E. Arimondo, and O. Morsch, "Full Counting Statistics and Phase Diagram of a Dissipative Rydberg Gas," Phys. Rev. Lett **113**, 023006 (2014).
[30] Michael Hoening, Wildan Abdussalam, Michael Fleischhauer, and Thomas Pohl, "Antiferromagnetic long-range order in dissipative Rydberg lattices," Phys. Rev. A **90**, 021603 (2014).
[31] N. Šibalić, C. G. Wade, C. S. Adams, K. J. Weatherill, and T. Pohl, "Driven-dissipative many-body systems with mixed power-law interactions: Bistabilities and temperature-driven nonequilibrium phase transitions," Phys. Rev. A **94**, 011401 (2016).
[32] F. Letscher, O. Thomas, T. Niederprüm, M. Fleischhauer, and H. Ott, "Bistability versus metastability in driven dissipative Rydberg gases," Phys. Rev. X **7**, 021020 (2017).
[33] Ricardo Gutiérrez, Cristiano Simonelli, Matteo Archimi, Francesco Castellucci, Ennio Arimondo, Donatella Ciampini, Matteo Marcuzzi, Igor Lesanovsky, and Oliver Morsch, "Experimental signatures of an absorbing-state phase transition in an open driven many-body quantum system," Phys. Rev. A **96**, 041602 (2017).
[34] Dong Yan, Binbin Wang, Zhengyang Bai, and Weibin Li, "Electromagnetically induced transparency of interacting Rydberg atoms with two-body dephasing," Opt. Express **28**, 9677–9689 (2020).
[35] Dong-Sheng Ding, Hannes Busche, Bao-Sen Shi, Guang-Can Guo, and Charles S. Adams, "Phase Diagram and Self-Organizing Dynamics in a Thermal Ensemble of Strongly Interacting Rydberg Atoms," Phys. Rev. X **10**, 021023 (2020).
[36] M. D. Lukin, M. Fleischhauer, R. Cote, L. M. Duan, D. Jaksch, J. I. Cirac, and P. Zoller, "Dipole Blockade and Quantum Information Processing in Mesoscopic Atomic Ensembles," Phys. Rev. Lett **87**, 037901 (2001).
[37] D. Tong, S. M. Farooqi, J. Stanojevic, S. Krishnan, Y. P. Zhang, R. Côté, E. E. Eyler, and P. L. Gould, "Local Blockade of Rydberg Excitation in an Ultracold Gas," Phys. Rev. Lett **93**, 063001 (2004).
[38] Kilian Singer, Markus Reetz-Lamour, Thomas Amthor, Luis Gustavo Marcassa, and Matthias Weidemüller, "Suppression of Excitation and Spectral Broadening Induced by Interactions in a Cold Gas of Rydberg Atoms," Phys. Rev. Lett **93**, 163001 (2004).
[39] Rolf Heidemann, Ulrich Raitzsch, Vera Bendkowsky, Björn Butscher, Robert Löw, Luis Santos, and Tilman Pfau, "Evidence for Coherent Collective Rydberg Excitation in the Strong Blockade Regime," Phys. Rev. Lett.

99, 163601 (2007).
[40] Tony E. Lee, Hartmut Häffner, and M. C. Cross, "Antiferromagnetic phase transition in a nonequilibrium lattice of Rydberg atoms," Phys. Rev. A **84**, 031402 (2011).
[41] Tony E. Lee, Hartmut Häffner, and M. C. Cross, "Collective quantum jumps of Rydberg atoms," Phys. Rev. Lett. **108**, 023602 (2012).
[42] Anzi Hu, Tony E. Lee, and Charles W. Clark, "Spatial correlations of one-dimensional driven-dissipative systems of Rydberg atoms," Phys. Rev. A **88**, 053627 (2013).
[43] Andrea Tomadin, Sebastian Diehl, and Peter Zoller, "Nonequilibrium phase diagram of a driven and dissipative many-body system," Phys. Rev. A **83**, 013611 (2011).
[44] Sven Zimmermann, Wassilij Kopylov, and Gernot Schaller, "Wiseman-Milburn control for the Lipkin-Meshkov-Glick model," J. Phys. A: Math. Theor. **51**, 385301 (2018).
[45] Julia Hannukainen and Jonas Larson, "Dissipation-driven quantum phase transitions and symmetry breaking," Phys. Rev. A **98**, 042113 (2018).
[46] João S. Ferreira and Pedro Ribeiro, "Lipkin-Meshkov-Glick model with Markovian dissipation: A description of a collective spin on a metallic surface," Phys. Rev. B **100**, 184422 (2019).
[47] Tony E. Lee, Ching-Kit Chan, and Susanne F. Yelin, "Dissipative phase transitions: Independent versus collective decay and spin squeezing," Phys. Rev. A **90**, 052109 (2014).
[48] B. Olmos, W. Li, S. Hofferberth, and I. Lesanovsky, "Amplifying single impurities immersed in a gas of ultracold atoms," Phys. Rev. A **84**, 041607 (2011).
[49] B. Olmos, D. Yu, and I. Lesanovsky, "Steady-state properties of a driven atomic ensemble with nonlocal dissipation," Phys. Rev. A **89**, 023616 (2014).
[50] C. D. Parmee and N. R. Cooper, "Phases of driven two-level systems with nonlocal dissipation," Phys. Rev. A **97**, 053616 (2018).
[51] Sebastian Diehl, Andrea Tomadin, Andrea Micheli, Rosario Fazio, and Peter Zoller, "Dynamical Phase Transitions and Instabilities in Open Atomic Many-Body Systems," Phys. Rev. Lett. **105**, 015702 (2010).
[52] J. von Boehm and Per Bak, "Devil's Stairs and the Commensurate-Commensurate Transitions in CeSb," Phys. Rev. Lett. **42**, 122–125 (1979).
[53] Zhihao Lan, Jiří Minář, Emanuele Levi, Weibin Li, and Igor Lesanovsky, "Emergent Devil's Staircase without Particle-Hole Symmetry in Rydberg Quantum Gases with Competing Attractive and Repulsive Interactions," Phys. Rev. Lett. **115**, 203001 (2015).
[54] P. Schauß, J. Zeiher, T. Fukuhara, S. Hild, M. Cheneau, T. Macrì, T. Pohl, I. Bloch, and C. Gross, "Crystallization in Ising quantum magnets," Science **347**, 1455–1458 (2015).
[55] Zhihao Lan, Igor Lesanovsky, and Weibin Li, "Devil's staircases without particle-hole symmetry," Phys. Rev. B **97**, 075117 (2018).
[56] Hendrik Weimer and Hans Peter Büchler, "Two-Stage Melting in Systems of Strongly Interacting Rydberg Atoms," Phys. Rev. Lett. **105**, 230403 (2010).
[57] Eran Sela, Matthias Punk, and Markus Garst, "Dislocation-mediated melting of one-dimensional Rydberg crystals," Phys. Rev. B **84**, 085434 (2011).
[58] David Petrosyan, "Two-dimensional crystals of Rydberg excitations in a resonantly driven lattice gas," Phys. Rev. A **88**, 043431 (2013).
[59] Zhihao Lan, Weibin Li, and Igor Lesanovsky, "Quantum melting of two-component Rydberg crystals," Phys. Rev. A **94**, 051603 (2016).
[60] Steven H. Strogatz, *Nonlinear Dynamics and Chaos: With Applications to Physics, Biology, Chemistry, and Engineering (2nd ed.)* (CRC Press, 2015).
[61] A. Piñeiro Orioli, A. Signoles, H. Wildhagen, G. Günter, J. Berges, S. Whitlock, and M. Weidemüller, "Relaxation of an isolated dipolar-interacting Rydberg quantum spin system," Phys. Rev. Lett. **120**, 063601 (2018).
[62] Chris Nill, Kay Brandner, Beatriz Olmos, Federico Carollo, and Igor Lesanovsky, "Many-body radiative decay in strongly interacting Rydberg ensembles," Phys. Rev. Lett. **129**, 243202 (2022).
[63] E.J. Robertson, N. Šibalić, R.M. Potvliege, and M.P.A. Jones, "ARC 3.0: An expanded Python toolbox for atomic physics calculations," Computer Physics Communications **261**, 107814 (2021).